remote sensing

MDPI

Article

Greening and Browning Trends on the Pacific Slope of Peru and Northern Chile

Hugo V. Lepage *, Eustace Barnes, Eleanor Kor, Morag Hunter and Crispin H. W. Barnes

Cavendish Laboratory, Department of Physics, University of Cambridge, Cambridge CB3 0HE, UK; eb651@cam.ac.uk (E.B.); mah1003@cam.ac.uk (M.H.); chwb101@cam.ac.uk (C.H.W.B.)
* Correspondence: hl407@cam.ac.uk

Abstract: Accurate detection and quantification of regional vegetation trends are essential for understanding the dynamics of landscape ecology and vegetation distribution. We applied a comprehensive trend analysis to satellite data to describe geospatial changes in vegetation along the Pacific slope of Peru and northern Chile, from sea level to the continental divide, a region characterised by biologically unique and highly sensitive arid and semi-arid environments. Our statistical analyses show broad regional patterns of positive trends in EVI, called "greening", alongside patterns of "browning", where trends are negative between 2000 and 2020. The coastal plain and foothills, up 1000 m, contain notable greening of the coastal Lomas and newly irrigated agricultural lands occurring alongside browning trends related to changes in land use practices and urban development. Strikingly, the precordilleras show a distinct 'greening strip', which extends from approximately 6°S to 22°S, with an altitudinal trend, ascending from the tropical lowlands (170–780 m) in northern Peru to the subtropics (1000–2800 m) in central Peru and temperate zone (2600–4300 m) in southern Peru and northern Chile. We find that the geographical characteristics of the greening strip do not match climate zones previously established by Köppen and Geiger. Greening and browning trends in the coastal deserts and the high Andes lie within well defined climatic and life zones, producing variable but identifiable trends. However, the distinct Pacific slope greening presents an unexpected distribution with respect to the regional Köppen–Geiger climate and life zones. This work provides insights on understanding the effects of climate change on Peru's diverse ecosystems in highly sensitive, biologically unique arid and semi-arid environments on the Pacific slope.

Keywords: MODIS; EVI; time series; Andes; climate zones; life zones; trend

Citation: Lepage, H.V.; Barnes, E.; Kor, E.; Hunter, M.; Barnes, C.H.W. Greening and Browning Trends on the Pacific Slope of Peru and Northern Chile. *Remote Sens.* **2023**, *15*, 3628. https://doi.org/10.3390/rs15143628

Academic Editor: Yongshuo Fu

Received: 26 April 2023
Revised: 15 June 2023
Accepted: 21 June 2023
Published: 21 July 2023

1. Introduction

Climatic conditions are considered to be the primary determinants of vegetation patterns, mediated by a complex of locally specific variables that significantly impact ecosystem services, from watershed protection and soil conservation to land use utility and resource availability [1,2]. The Köppen–Geiger climate classification model is based on the ambition to understand what determines the types of vegetation that could be found in any given region [3,4]. It is a widely used system that divides climates into five principal groups (tropical, arid, temperate, continental and polar), each sub-divided according to rainfall and temperature data to provide thirty discrete climate zones [3]. The Köppen–Geiger system produces geographical zones strongly linked to vegetation productivity and the geographical determinants of plant diversity, which makes it particularly useful in understanding and predicting regional changes in the distribution of life zones [2,5]. It is the dynamic character of climatic conditions that produces long-term changes in vegetative distribution [6–8]. This complex interaction significantly impacts environmental processes that determine ecosystem services and resource availability. Globally, climate change is increasingly considered to be one of the greatest threats to environmental systems and ecosystem services, with biodiversity being particularly vulnerable [9–12]. Atmospheric

CO_2 concentration, the primary limiting factor of photosynthesis, has risen from 277 ppm in 1750 to 414.35 ppm in 2022 [13] and is predicted to continue rising [14–16]. Increasing atmospheric CO_2 concentration is understood to enhance water efficiency in photosynthetic processes, relaxing ambient limits to plant productivity, especially in semi-arid regions [17]. In combination with atmospheric CO_2 concentration, moisture availability and temperature are also key factors for determining vegetation productivity. While spatial changes in rainfall and temperature are highly variable, the general easing of limiting factors for photosynthesis is now considered to be causing global greening [5,18].

The climatic drivers of spatio-temporal vegetation dynamics are not well understood in mountainous regions [19,20]. Arid land habitats in upland regions are considered to be more sensitive to changes in climatic variables than habitats in more humid regions, with minor changes in the climatic drivers having a proportionately greater impact in such habitats [17,21,22]. Loss of habitat driven by climate change, especially for endemic organisms in these highly specialised environments, lends increasing justification to the monitoring of environmental change in arid mountainous regions [20]; however, few regional studies of vegetation dynamics in arid upland regions have been conducted [23,24].

As in many regions of the world, environmental change in the Andes is generally associated with deforestation, long-term habitat degradation and large-scale infrastructural projects [25,26]. The Pacific slope of the Andes in Peru and northern Chile is of particular interest and offers a crucial study area for examining vegetative response to climate change for four main reasons: 1. the region is both arid and mountainous, with the Andes rising rapidly from the arid coastal plain to 6000 m at the continental divide, and is only dissected by rivers that cut deep east–west valleys running to the Pacific Ocean; 2. while the region supports relatively low levels of biodiversity, it is characterised by environmental fragility and high levels of biological endemism, with four discrete centres of endemicity [27–30]; 3. the region is characterised by sharp east–west humidity and temperate gradients, producing distinct vegetation zones that, in large part, remain natural or semi-natural and 4. the Pacific slope is a highly vulnerable and water-scarce region with significant pressures on natural resources from several large cities in the coastal deserts, including Lima, Trujillo and Arequipa in Peru to Antofagasta and Calama in northern Chile, which are totally dependent on scarce water resources available in this region [31–33]. An understanding of the spatio-temporal responses to climate change in the region is, therefore, vital in predicting the impacts of climate change on ecosystem services and resource availability while conserving biological endemism [11].

Of the climatic variables that determine photosynthetic productivity, temperature, moisture availability and atmospheric CO_2 concentration are widely considered the most important [34–36]. Temperature declines by approximately 1 °C with each 100 m of ascent, progressively imposing a limit to photosynthetic productivity as elevation increases. Photosynthetic CO_2 uptake potential is known to decline with increasing altitude as temperature falls [37], while CO_2 concentration is more evenly distributed throughout the troposphere. However, below 800 m asl, but only up to 300 m above any given point, CO_2 concentration is more variable. This is related primarily to plant productivity and is enhanced in regions characterised by semi-permanent atmospheric stability, as in this region [38]. Precipitation and moisture availability show high regional heterogeneity across the Pacific slope of Peru [39]. This is largely determined by seasonality, altitude, aspect and atmospheric stability and is significantly impacted by the episodic El Niño phenomenon, although there appears to be a nonlinear relationship between rainfall and El Niño events [40].

Plant physiologist Wladimir Köppen was instrumental in developing the widely used Köppen–Geiger climate classification system and motivated by his interest, as a botanist, in the climatological determinants of plant distributions [3]. Recently revised and updated, this model is based on climate data, which, given its connection to plant life, can be used to analyse and predict the impact of climate change on plant distributions [2,4]. Wladimir Köppen first divided vegetation zones into five broad categories, determined by combining temperature and precipitation thresholds to provide equatorial, arid, warm temperate,

snow and polar climates coded A, B, C, D and E, respectively. Each of these groups is then further divided using seasonal precipitation patterns and then again according to temperature thresholds to produce thirty distinct climate zones [2,4].

The Pacific slope of Peru and northern Chile falls into four of these climate zones, listed in Table 1 and shown in Figure 1. This includes the arid, hot deserts (coded BWh), which stretch discontinuously south along the coastal deserts, from northern Peru to northern Chile, with a climate defined by monthly average temperatures exceeding 10 °C and over 50% of its precipitation falling in a short wet season. Highly sensitive floristic assemblages in this zone are largely restricted to narrow riparian strips that cross the coastal deserts as well as the numerous coastal wetlands. The arid, cold desert region (coded BWk) lies above the hot deserts and extends from northern Peru to Chile. This region, as defined by Köppen, gradually expands to the south along the Pacific slope to become the dominant climatic zone at lower elevations in southern Peru and northern Chile. This zone differs from the hot deserts in having at least one month in which average temperatures lie below 0 °C. Vegetation in this zone is also sparse but locally more prolific in the fog oases or Lomas. Above the cold desert lies the cold semi-arid steppe (coded BSk), which extends along the Pacific slope in a narrow elevational strip that gradually ascends southwards into Chile and Bolivia. This zone differs from the cold deserts in that more than 50% of its precipitation falls outside a short wet season and is characterised by dense thorn scrub and cacti. It is this zone that harbours much of the region's biological endemicity, together with transitional cold desert vegetation grading into BSk [27]. Ascending to the high Andes, the cold semi-arid steppe climate zone gives way to the polar tundra (coded ET). This is a more simply defined climate with average monthly temperatures lying above freezing but not exceeding 10 °C and being a region typically covered in open Puna grasslands with relictual patches of Polylepis woodlands. The hot arid steppe zone (BSh) only occupies a very small and fragmented area above hot deserts in the far north of Peru. As our area of interest lies to the south, this climate zone does not appear in our analysis. When mapped, these climatic zones produce a north to south arrangement of parallel zones following the Pacific slope of Peru and northern Chile as shown in Figure 1, which indicates our study area and the major Köppen–Geiger climate zones [3,4].

The use of time-series satellite data for remote sensing has developed rapidly since their inception, providing a powerful set of tools to monitor geospatial and temporal changes at Earth's surface [41]. A large number of studies looking at regional and global changes in photosynthetic productivity at Earth's surface are allowing for ever more sophisticated analyses of regional patterns of greening and vegetation dynamics [17,42]. While it is generally accepted that global 'greening' is taking place, primarily driven by increasing atmospheric CO_2, regional patterning of vegetation response is more complex, especially in mountainous regions [17,43]. Studies have also indicated that research in discreet regions might reveal previously undetected trends and that these would most likely be in mountainous regions since sharp elevation gradients can mask trends [43]. A standard metric for measuring the health and abundance of vegetation is the normalized difference vegetation index (NDVI), which is based on the principle that photosynthetic activity in plants will absorb red light and reflect infrared light in healthy plants, while the opposite holds for unhealthy plants, where photosynthesis reduces or does not take place [44]. The NDVI is then derived as the normalized ratio of reflectance between red and infrared wavelengths for terrestrial surfaces. Where photosynthetic processes are increasing plant growth, an NDVI time series exhibits a positive trend known as 'greening' or a negative trend and known as 'browning', where plant growth is decreasing. The NDVI is strongly influenced by atmospheric aerosol loading, the angle of solar incidence, time of day and soil conditions, all of which variably distort values [45]. The Enhanced Vegetation Index (EVI) modifies the NDVI, optimising vegetation signals by correcting for these distortions using blue wavelengths to correct for atmospheric aerosols and a canopy background adjustment factor. The two vegetation indices together provide a

highly reliable and robust means of analysing vegetation and have been widely used in studies of vegetation trends at a variety of scales across the globe [17].

Table 1. Study area composition, as defined by Köppen–Geiger zones [4], totalling over 99% of the area. The climate zone code relates to the legend in Figure 1. We limited our study to the Pacific slope of the Andes, excluding climate zones on the eastern side of the continental divide, coloured in light gray.

Climate Zone	Code	Area Coverage
Arid, Desert, Cold	BWk	30.0%
Polar, Tundra	ET	29.2%
Arid, Desert, Hot	BWh	16.7%
Arid, Steppe, Cold	BSk	7.9%
Temperate, no dry season, warm summer	Cfb	6.1%
Temperate, dry winter, warm summer	Cwb	5.2%
Tropical, savannah	Aw	2.0%
Arid, steppe, hot	BSh	1.3%
Tropical, rainforest	Af	0.9%

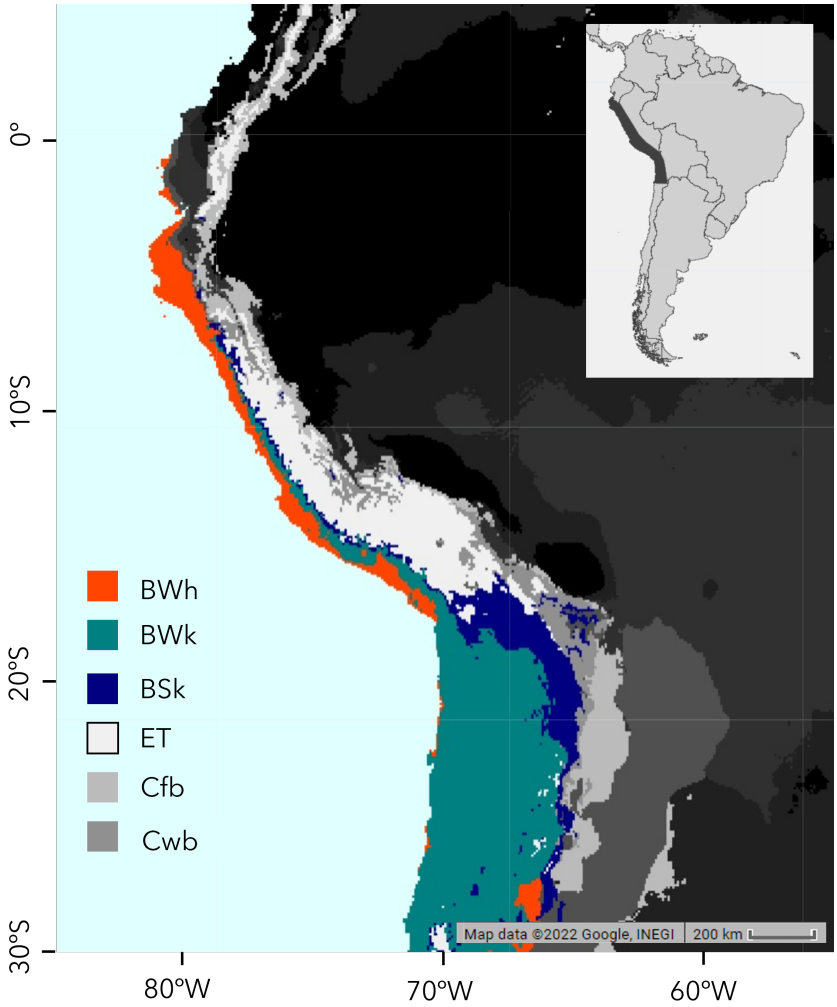

Figure 1. EPSG:4326 projection of the South American Andes with colour-coded climate zones [4]. The key for the legend is found in Table 1. The darker shaded area in the inset represents the region of interest for which we processed satellite data.

Huete et al., 2006, using the EVI, analysed trends across the Amazon basin, identified counterintuitive dry season greening, igniting a debate about the veracity of the method and the variable impact of regional drivers of vegetative productivity [46]. Long-term regional studies, driven by the need to understand the impacts of climate change on the vegetation dynamics in the circumpolar boreal forests and Arctic region, have also been widely undertaken [47–49]. At a more regional scale, Aide et al., 2019 identified geospatial greening patterns in the Andes, in which woody vegetation decreased between 1000–1500 m but increased above that elevation [50]. Analyses of greening patterns in the Andes and European Alps have further demonstrated the value of NDVI and EVI for monitoring trends in the retreat of ice sheets [49,51]. More complex studies have analysed geospatial trends in biologically diverse and topographically complex regions from the Himalaya [19] and Andean cordilleras [52] to Peru [52]. While most studies have employed NDVI, the EVI is increasingly viewed as a more sensitive and robust measure of vegetative productivity [53].

Although studies have been undertaken regarding climate change impacts on vegetation dynamics in the highly biodiverse, but sparsely populated, Amazon basin, there are few such studies of the Pacific slope of the Andes despite high levels of biological endemism in the region and extreme urban vulnerability to water scarcity [12,46,52,54,55]. This important region is characterised by highly variable geospatial contrasts in human impact and vegetation. The coastal valleys up to 1200 m asl are being intensively developed, while the valleys from 1200–3500 m asl are farmed less intensively and the steeper slopes of the Andes, covering much of the region, above 1200 m are being used only for extensive grazing [27,50]. Given dramatic environmental gradients in the Andes of the Pacific slope, with highly structured climatic zonation related to both moisture availability and elevation from west to east and a strong north–south moisture gradient, it is likely that climatic drivers will have a highly differentiated geospatial impact on vegetation dynamics, a pattern further complicated by the combination of isolated sub-regions of biological endemism and distinctive vegetative assemblages together with complex patterns of anthropogenic pressures. This presents a complex interpretive challenge, requiring smaller-scale studies across the entire Pacific slope of Peru and northern Chile to fully understand the impacts of climate change here. At present, there remains a gap in our knowledge not only of the response to climatic drivers across these environmental gradients but also of the habitats and ecosystem dynamics on the Pacific slope [27].

In this study, we have carried out a trend analysis of MODIS time-series multi-spectral imagery from 2000 to 2020 as a proxy for vegetation productivity to identify geospatial greening and browning trends for the Pacific slope of Peru and northern Chile. We verify the statistical significance of remotely sensed data to produce a clear pattern in vegetation response and validate our observations with much needed ground-truthing fieldwork. We discuss causation of greening patterns, correlating calculated vegetation response with known climatic drivers and the geospatial patterning identified by the Köppen–Geiger climate classification system in the region. Thus, we are proposing that greening patterns will be largely determined by climatic drivers and mirror the climate classification zonation of the Köppen–Geiger climate model.

2. Materials and Methods

2.1. Study Area

This study is focused on the arid Pacific slope of South America between 6°S and 22°S, extending from Chiclayo in northern Peru south to Calama in northern Chile and bounded by the Pacific Ocean to the west and the continental divide to the east; in total, it is an area of 50,406 km^2. Figure 1 shows the study area and major climate zones, as defined by the Köppen–Geiger climate classification model [3,4]. In our area of interest, greening data were principally analysed over four climate zones: the hot arid desert (BWh), cold arid desert (BWk), cold arid steppe (BSk) and polar tundra (ET). The precise area coverage of each climate zone is shown in Table 1. Although some of our satellite images have included

tropical rainforest, we restrict our studies to the Pacific slope of the Andes, which does not contain rainforest climate zones in Peru. Within these climate zones, what we refer to as the 'greening strip' is almost entirely confined to the hot and cold arid deserts and the cold arid steppe.

The abrupt rise in the Andes from sea level to 6786 m in this region combines a unique blend of climatic and vegetation types and land use patterns from west to east and north to south [56,57]. The climate along the Pacific slope is strongly influenced by the Intertropical Convergence Zone (ITCZ), the episodic El Niño Southern Oscillation (ENSO) phenomenon in combination with the cold Humboldt current and orographic influence of the Andes, producing great spatial variation in both temperature and precipitation. Regional precipitation patterns are highly variable, especially in the context of the El Niño Southern Oscillation. However, precipitation on the arid pacific slope typically ranges from 50 mm/year in the northern coastal deserts to 0 mm/year in the south [58]. At higher elevations up to the continental divide, precipitation ranges up to 1000 mm/year [59]. The marked spatial variation in the distribution of precipitation is primarily due to steep west–east altitudinal gradients, which consequently control the distribution of vegetation zones, maintaining a significant environmental diversity.

The arid and hyper-arid coastal deserts of Peru and Chile are bisected by numerous broad river valleys and associated riparian vegetation with a series of coastal Lomas or fog oases on the coastal hills from Trujillo southwards. In the dramatic transition from the coast through the arid sub-tropics, vegetative associations grade from thorny cactus scrub to dry shrubby woodlands at 2500 m [60]. In turn, this grades to a complex mix of relictual polylepis woodlands, puna grasslands and peatlands (wetlands) to the arctic-alpine zone above 5100 m, rising locally to over 6500 masl in the Cordillera Blanca and Cordillera Occidental.

2.2. Remote Sensing Data

In this analysis, we used the EVI dataset of the Terra module of the Moderate Resolution Imaging Spectroradiometer (MODIS) sensor as a proxy for land condition changes [61]. The dataset used is the MOD13Q1.006 Terra Vegetation Indices 16-Day Global 250 m resolution provided by NASA LP DAAC at the USGS EROS Center [53,62]. This dataset creates a composite image of Earth by integrating the best-quality images from a 16-day period, with each pixel marked with an overall quality indicator. We chose MODIS as it offers a reliable dataset over the past two decades, with any systematic errors being consistent for each data point as part of the updated Collection 6 [53,62,63]. The MODIS image collections were accessed and pre-processed using the Google Earth Engine platform [64]. Changes to the EVI were investigated over a twenty-one year period from the beginning of 2000 to the end of 2020.

Our interest in climatically driven greening across the Pacific slope required that we differentiate direct anthropogenic effects, such as urban development and agricultural expansion, on the vegetation signal from broader biogeographical outcomes emergent from global or continental changes. It has been previously noted that the strong greening hot spots in the arid lands are primarily of human causation [52]. It is certainly agreed that the expansion of croplands can be reliably detected with vegetatyion indices EVI and NDVI [17]. Specific EVI returns can indicate direct land cover change resulting from human activity, and these were used in combination with positive field verification from satellite images to determine and confirm direct change. Direct anthropogenic land cover change can be both permanent or semi-permanent and is uniquely identifiable. For example, recently irrigated farmlands appear as patchworks of rectangular greening corresponding to fields being watered. Where irrigation has ceased, such rectangular areas appear patchy and browning as the photosynthetic capacity of the field diminishes unevenly. In the same way, regularly shaped areas of extreme browning are indicative of more recent land cover transformation resulting from the construction of houses or factories and corresponding largely to urbanisation. Verifying that these extremes of land cover change corresponded

to discrete greening or browning driven by human activity is increasingly viewed as an essential component in the drive to identify, confirm and understand regional biogeographic change [17]. Our field verification was undertaken in the departments of Lima and Moquegua in Peru in the Fortaleza, Pativilca, Cañete and Moquegua drainage basins from 2017 to 2022, supported with reference to Google Earth satellite imagery.

2.3. Data Analysis Workflow

Figure 2 details our workflow for data extraction and analysis. We separate our work into three main parts: the pixel-by-pixel analysis of the 20-year time period, the construction of spatially averaged time series and statistical correlations with climate factors.

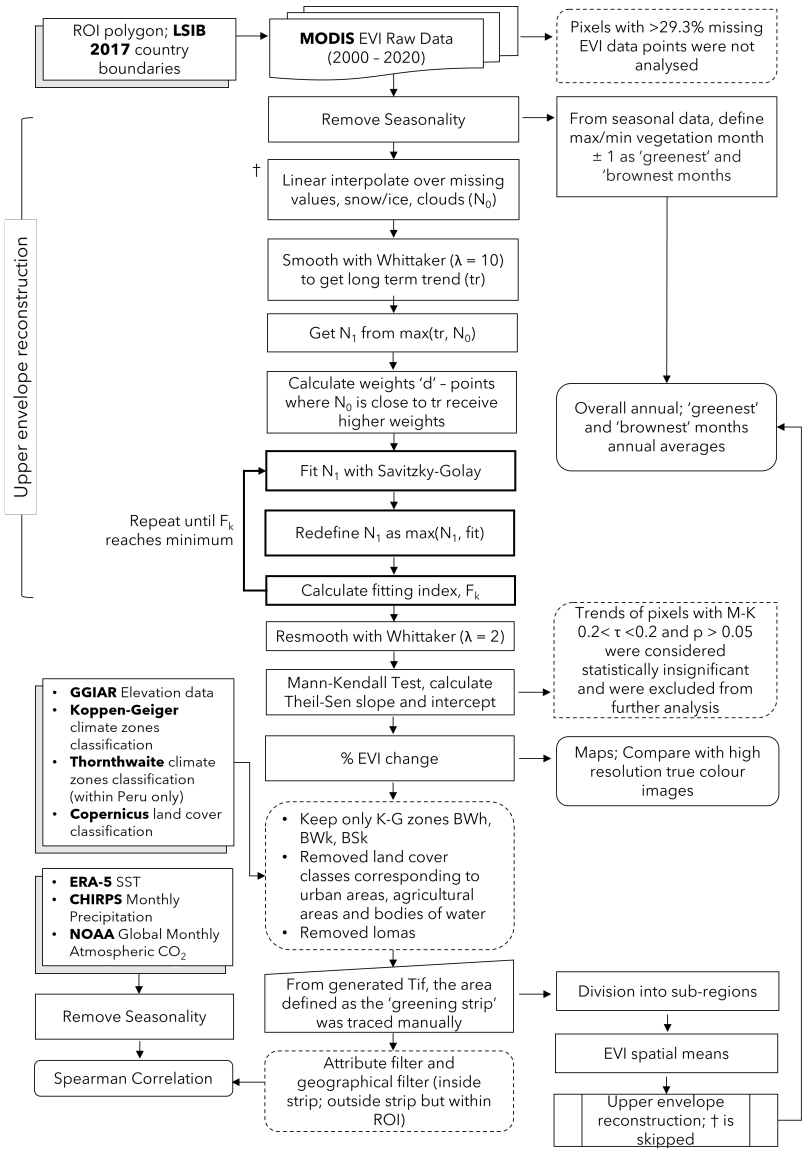

Figure 2. MODIS imagery analysis workflow. Boxes with shadows represent inputs from other datasets. Boxes with rounded corners represent final results. Boxes with dotted outlines represent steps where data are discarded or excluded from analysis. Bolded outlines are repeated processes. The abbreviations used in this workflow are for the Large Scale International Boundary (LSIB), the Mann–Kendall test (M–K), the European Centre for Medium-Range Weather Forecasts reanalysis (ERA-5), the Climate Hazards Group InfraRed Precipitation with Station (CHIRPS), the National Oceanic and Atmospheric Administration (NOAA) and the Consultative Group for International Agricultural Research (CGIAR).

2.4. Pixel Pre-Processing

Raw EVI data were obtained from MODIS at 250 m × 250 m resolution [62]. We have also performed this analysis using NDVI rather than EVI and have obtained the same results. For the sake of clarity, we only present EVI data in this paper. In this study, we refer to 'pixels' as geographical points spaced approximately 250 m by 250 m apart. 'Points' refer to single 16-day composite, temporal data points in the time series of each pixel. Points are classified within the MODIS dataset as missing, good, marginal, snow/ice and clouds in the 'SummaryQA' band and labelled $-1, 0, 1, 2$ and 3, respectively [65]. Pixels where more than 29.3% of EVI data points were missing were not analysed because, below this threshold, a Theil–Sen regression can no longer be considered robust [66]. To ensure that the time series can be compared with an equal frequency, missing temporal data points were filled in using linear interpolation.

2.5. Seasonal Decomposition

In order to extract yearly and periodic vegetation index fluctuations, the complete time series for each pixel was decomposed using additive decomposition, which resulted in three time series patterns: trend, seasonal and residual components. We used the `statsmodels.tsa.seasonal.seasonal_decompose` python package [67] Release 0.11.0. The seasonal component was removed using a periodicity of 23 points per year, preserving the trend and residual components. The residual component was not removed at this stage because the package employs a self-reportedly naïve method of extracting the trend, leaving a result that is too smooth and removes all finer details from the time series [67].

2.6. EVI Upper Envelope Calculation

Cloudy days and poor atmospheric conditions will negatively affect the EVI and produce a false reading of degraded vegetation health. To minimize this effect, we take the upper envelope of our entire time series. The methodology, based on an improved Savitzky–Golay filter, is largely adapted from Chen et al. [68].

We used linear interpolation to replace data points that were classified as snow/ice, clouds and points that corresponded to missing EVI; this was defined as N^0. The completed series was then smoothed using Whittaker smoothing [69], a version of spline smoothing for discrete series with smoothing parameter $\lambda = 10$. The smoothed series was defined as N^{tr}. N^0 and N^{tr} were compared, and a new time series N^1 was defined where $N_i^1 = \max(N_i^0, N_i^{tr})$. This removed the downward spikes where EVI is underestimated due to clouds. The absolute difference between N^0 and N^{tr} is defined as $d_i = |N_i^0 - N_i^{tr}|$, with the maximum difference calculated as $d_{\max} = \max(d_i)$. The fitting weights are calculated using

$$W_i = \begin{cases} 1, & \text{when } N_i^0 \geq N_i^{tr} \\ 1 - d_i/d_{\max}, & \text{when } N_i^0 < N_i^{tr} \end{cases}. \quad (1)$$

A new upper envelope time series is defined as the highest value between the original time series and a fitted time series using the Savitzky–Golay (Sav–Gol) fitting; we label this time series N_i^{fit}. We define this new envelope as $N_i^k = \max(N_i^0, N_i^{fit})$.

A fitting index was calculated using

$$F_k = \sum_{i=1}^{n} |N_i^k - N_i^0| \times W_i \quad (2)$$

Iteratively fitting N^k and calculating F_k led to the exit condition $F_{k-1} \geq F_k \leq F_{k+1}$, i.e., minimum F_k being reached. The expected behaviour of the iteration fit curve is that F will decrease to a minimum and then increase, which typically takes 2 iterations. The fit corresponding to F_k was taken. For the Savitzky–Golay fitting, combinations of window length and poly-order from m = 5, 7, 9, 11, 13, 15, 17 and d = 2, 3, 4, 5, 6 with the condition

m > d were tested. It was found that m = 9, d = 6 was the combination that most consistently produced this behaviour.

For atypical cases:

- if $F_0 \leq F_1$, i.e., the iteration fit curve continually increased, the fit of the first iteration was taken,
- if, after 10 iterations, the $F_{k-1} \geq F_k \leq F_{k+1}$ condition was not met, i.e., iteration fit curve continually decreased, the fit of the last iteration was taken.

2.7. Assessment of Statistical Significance

The final fit from the Savitzky–Golay filtering was smoothed again using a Whittaker smoothing parameter of $\lambda = 2$. While $\lambda = 10$ was chosen earlier to produce a very smooth time series representing the long-term trend, $\lambda = 2$ was chosen to reduce the amount of noise remaining from the construction of the upper EVI envelope without removing details in each time series. The Whittaker filter was chosen over Savitzky–Golay because the Savitzky–Golay filter is less reliable at the start and end of the time series due to windowing effects and is, therefore, considered less robust [70].

The trend in our post-processed time series was assumed to be linear owing to the relatively short temporal observation window, and the Mann–Kendall test [71,72] (τ rank correlation) was used to determine its statistical significance. The slope and intercept were determined using the Theil–Sen estimator [73,74], with the intercept calculated using the Conover method [75]. This was completed using the `pymannkendall` package [76]. The criteria $\tau > 0.2$, $p > 0.05$, $\text{sign}(\tau) = \text{sign}(\text{slope})$ were used to qualify significantly greening and browning pixels.

To calculate relative EVI change (Δ_{EVI}), the trend was extrapolated to the first point of the time series; this is because `seasonal_decompose` truncates the beginning and end of the time series when returning trend and residual components.

$$\Delta_{\text{EVI}} = \frac{\text{slope} \times (\textbf{len}(\text{time series}) - 1)}{\text{intercept} - \text{slope} \times \textbf{len}(\text{truncated points})} \tag{3}$$

Values of this extrapolated 'initial EVI' between 0 and ± 0.000001 were set to ± 0.000001 to prevent division by 0 errors. For our analysis, only pixels with EVI change between -200% and 200% were considered; changes outside this range were assumed to be unnatural or caused by a very weak initial EVI value, possibly due to the presence of water or ice.

2.8. Spatially Averaged Time Series

Direct anthropogenic land cover changes relating principally to irrigation schemes and urban expansion were excluded from the analysis. The 31 March 2021 Land Cover Classification System (LCCS) developed by the Food and Agriculture Organisation (FAO) identifies these areas that were spatially excluded from our analysis [77].

Only statistically significant trends, as described in Section 2.7, were included in our time series analysis. We manually outlined a continuous area extending from northern Peru to northern Chile that exhibited high values of relative greening (approx. above 15%), which we define as the greening strip (GS). In order to compare the ecological dynamics of the greening strip with expected climatic behaviour, we divided the strip into the three climate zones that extend the area, namely the hot arid desert (BWh), the cold arid desert (BWk) and the cold arid steppe (BSk). We investigate the EVI time series for each climate zone both within the greening strip and over our entire area of study.

To construct our time series, we take the average EVI of all included pixels within a particular region for each point in time. The months corresponding to maxima and minima of the seasonal component were found and the 'greenest' and 'brownest' months were defined as the month before, during and after these maxima and minima, respectively. The average EVI values over the greenest and brownest months were compared to the overall annual average.

2.9. Statistical Correlations

Monthly precipitation values were obtained from CHIRPS [78] daily data monthly averages for each region. Sea surface temperature (SST) was obtained from Copernicus ERA-5 (reanalysed) [79] as a spatial average over a rectangular area between 6°S and 30°S and 70°W and 80°W. This area captures broad regions of the Pacific ocean affected by the Humboldt current. As with the EVI data we collected, seasonality was removed from these datasets prior to calculating a correlation. Monthly average CO_2 data (as a trended series without seasonality) were obtained from NOAA [80]. Assuming that vegetation does not respond to climate variations instantly, we allowed for a delayed response of up to 1 month for precipitation and up to 12 months for SST and CO_2. By adjusting this delay, we calculated the maximum correlation between each region's EVI time series and the above datasets. Longer delay times were not considered for precipitation data because most of the study area consists of plants that respond to precipitation in a matter of weeks. It was assumed that soil moisture would have negligible effect due to the aridity of the area. The maximum correlations between EVI series of each pair of regions were calculated, with delays of up to 12 months in both directions in time.

3. Results

We observe a complex spatially differentiated pattern of changes in EVI on the Pacific slope of Peru and northern Chile over a period from 2000 to 2020, with discrete zoning of greening and browning throughout the region. Figure 3 illustrates this patterning, and most notably a 'greening strip' that extends along the pacific slope, an area characterised by arid and hyper-arid climatic conditions. The EVI in this 'greening strip', highlighted in the inset of Figure 3, has increased by 15% during this period and extends from northern Peru to northern Chile and constitutes a hitherto undescribed novel phenomena.

There is an overall greening throughout the Andes from the foothills to the continental divide, while, in the coastal deserts, there is a mix of greening and browning, with significant areas that show no change. Figures 4–8 show six different areas of the greening strip in greater detail. These areas span the entire greening strip from northern Peru to northern Chile. The higher-resolution images presented in these figures reveal distinct polygons of urban areas that appear bright red or irrigated fields that appear bright green or red (depending on whether they have recently been irrigated or have been abandoned), while the natural vegetation changes are at a lower colour intensity and the boundaries less clear cut.

Strikingly, there is a regional gap in the greening strip on the coastal pre-cordilleras in central Peru (see Figure 4). However, the 'greening' would appear to be offset eastwards to the west facing the foothills of the Cordillera Blanca rather than the Cordillera Negra. This does reflect the geography of the region, with the Cordillera Negra running north–south in parallel with the much taller Cordillera Blanca to the east. The Southern Cordillera Blanca is a small area of high peaks.

Atmospheric circulation drives the easterly flowing air masses over the Andes. In this region, the taller peaks of the Cordillera Blanca (nearly 7000 m peaks) and Huayhuash force greater altitudinal uplift and vertical compression of airmasses than to the north or south. Air mass compression thus clears the Cordillera Negra, leaving it a relatively drier range with a noticeably more arid coastal strip. The greening is then recorded on the lower slopes of the Cordillera Blanca, southern Cordillera Blanca, upper Rio Fortaleza and Cordillera Huayhuash.

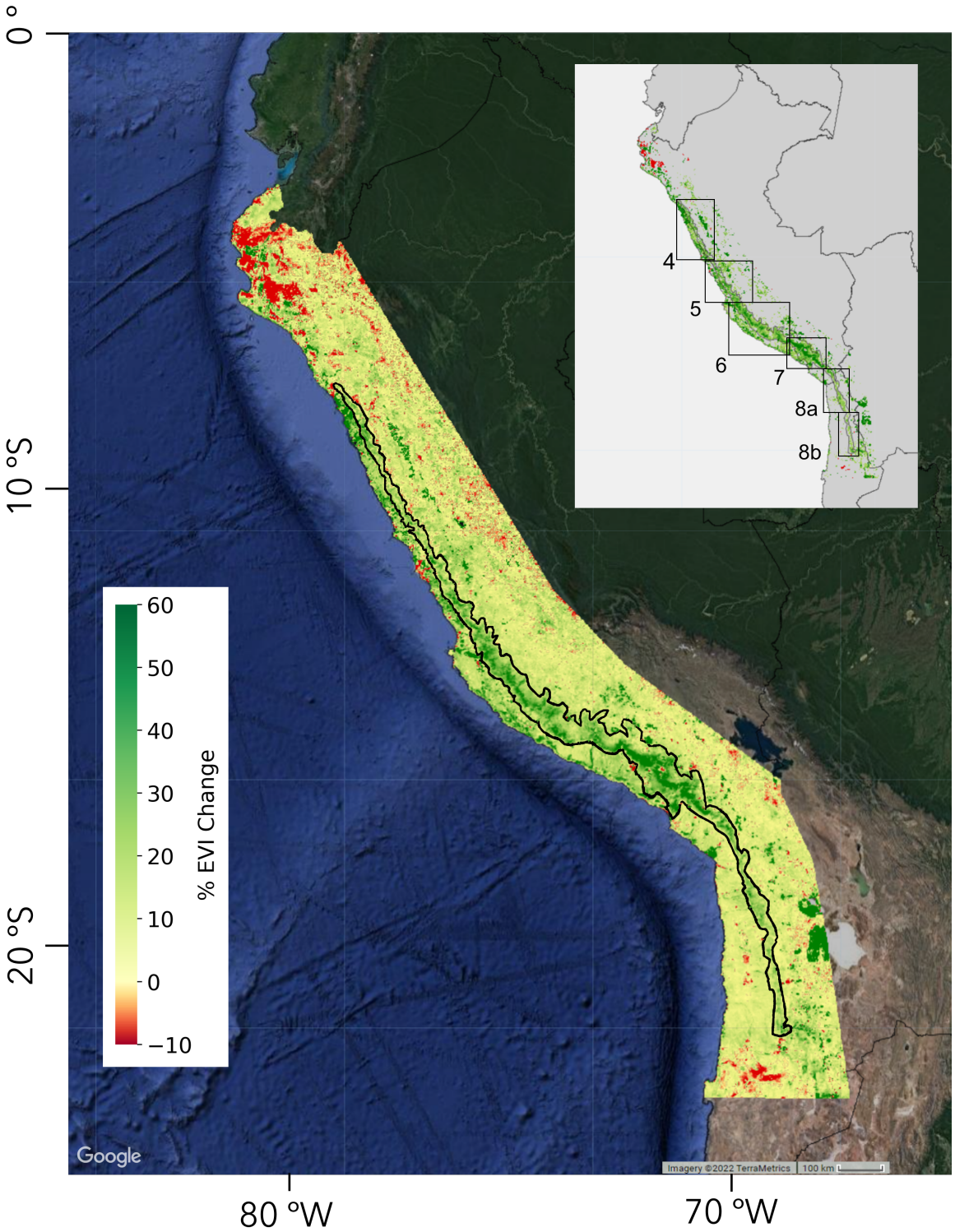

Figure 3. The area defined as the greening strip, outlined in black, extends from approximately 7.5°S to 22.5°S, located on the western flank of the Andes. The colour range includes pixels with EVI change between −10% and 60%, where changes below −10% and above 60% were clipped. The inset shows statistically significant pixels only, with an EVI change of at least ±15%. Rectangular outlines in the inset show locations for higher-resolution images that follow in Figures 4–8.

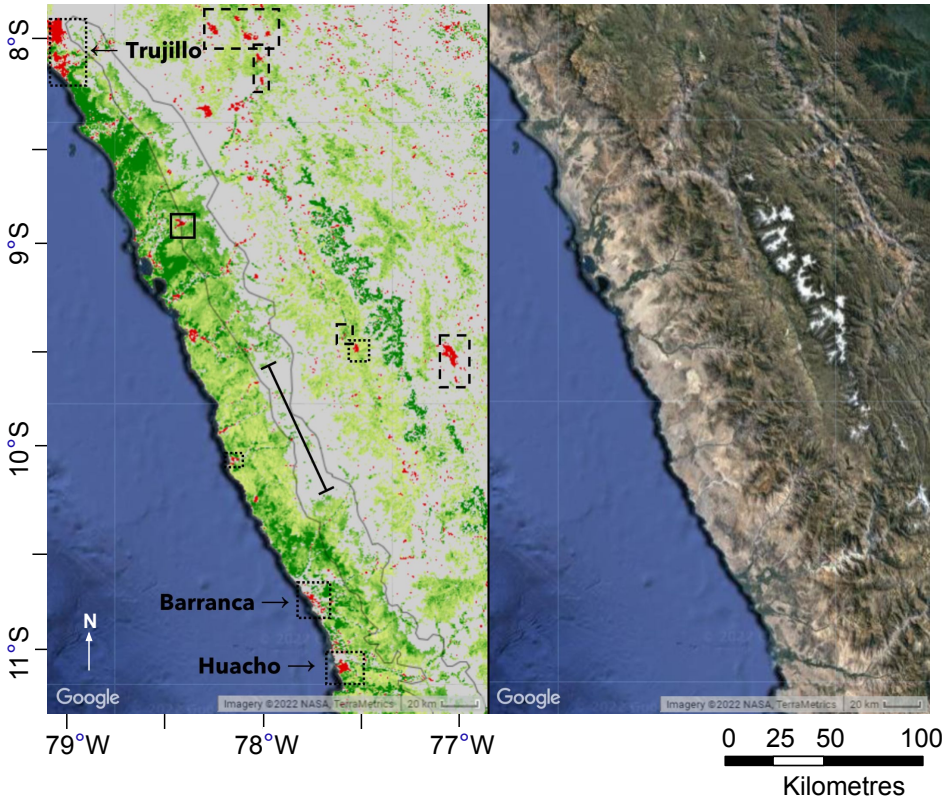

Figure 4. There is a greening gap from approximately 9.6°S to 10.2°S. Dotted outlines denote urban areas, dashed outlines denote mines and quarries, solid outlines represent agricultural areas. Unmarked large dark green areas along the coast and smaller red areas are linked to agriculture; these were excluded from the 'greening' strip. The dark green area towards the right hand side marks the outline of glaciers.

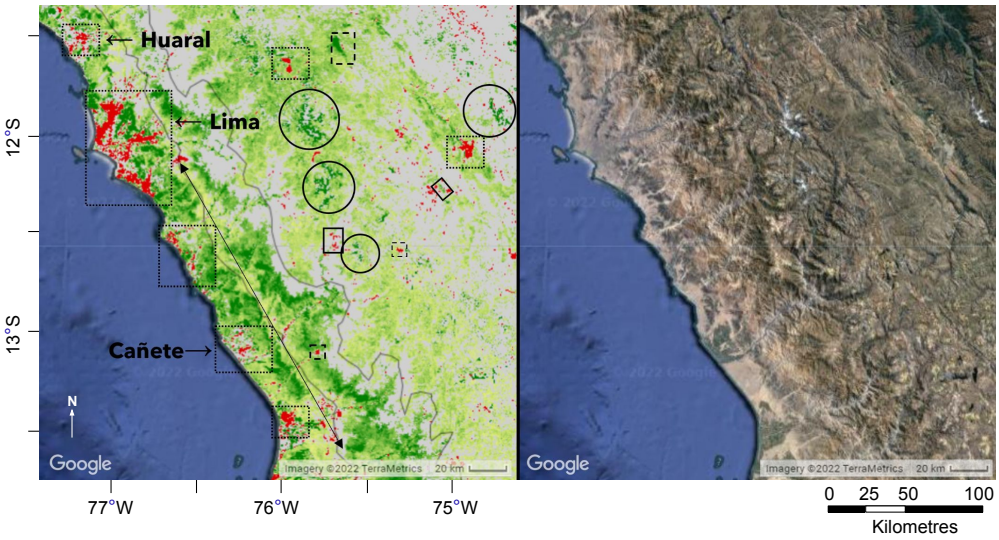

Figure 5. Greening increases in intensity southwards from Lima. Dotted outlines denote urban areas and dashed outlines denote mining activity. Areas of mining can appear as greening if they are abandoned or involve processes that deliver surface water where there was none previously. The solid tipped arrow represents separation between the strip and other less intense natural greening closer to the coast. The smaller coastal greening is located in a different geographical region and was not included in what we define as the greening strip. Red patches observed on the coast are urban areas. Red lines crossing the strip are roads and green lines are rivers. Solid outlines denote agricultural and farming areas.

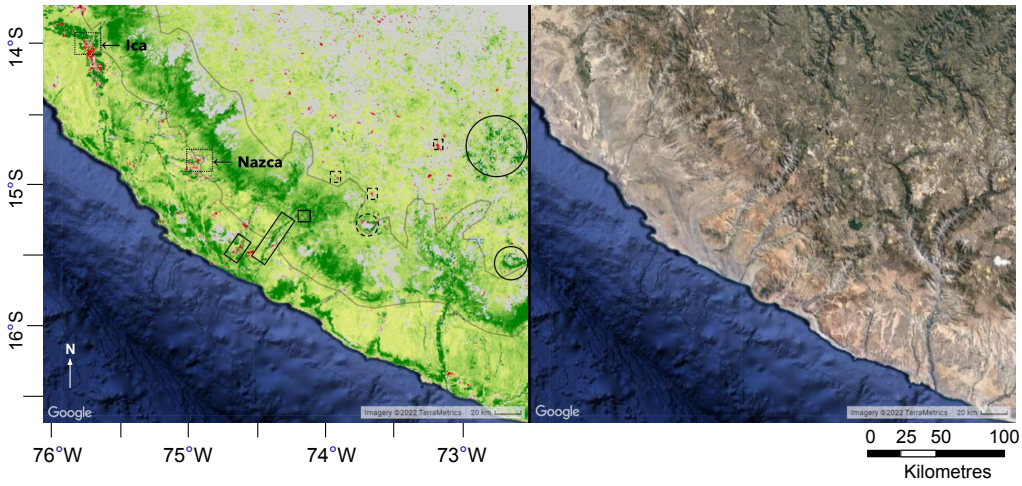

Figure 6. Dotted outlines denote urban areas and dashed outlines denote mines and quarries. The discontinuous areas of coastal greening were not included in the greening strip as they are located beneath the Pacific slope, sensu strictu. Agricultural development along rivers, highlighted using a solid box, was also excluded from our statistical analysis since any change in vegetation would be directly controlled by human activity. Similarly, red stripes perpendicular to the coast going into the strip are either roads or abandoned or less productive fields along rivers and were excluded from our analysis. Solid circles outline glaciers and solid outlines represent agricultural areas.

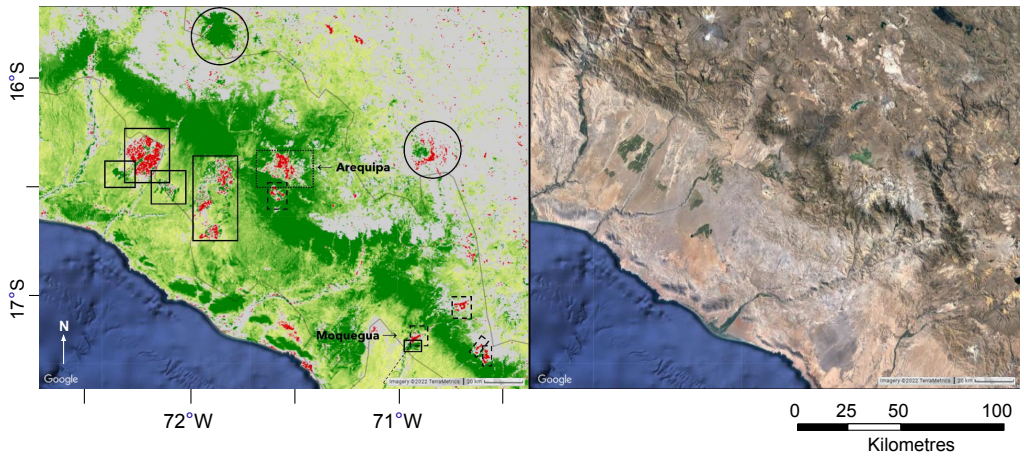

Figure 7. Dotted outlines denote urban areas, dashed outlines denote mines and quarries, and solid outlines represent agricultural areas. Larger red patches correspond to areas of urbanisation and changes in agricultural areas. The largest red patch in the above image is the Majes irrigation project, where a combination of changes in crops and reduced irrigation have produced marked browning more recently. The large marked red/green patches indicated are areas responding to direct human action and have been excluded from our analysis. Where browning is indicated, red or green lines extending from the coast up into the greening strip are rivers and roads. Pixels within the greening strip exhibit the most intense relative increase in the area located between Arequipa and Moquegua. Solid circles outline glaciers.

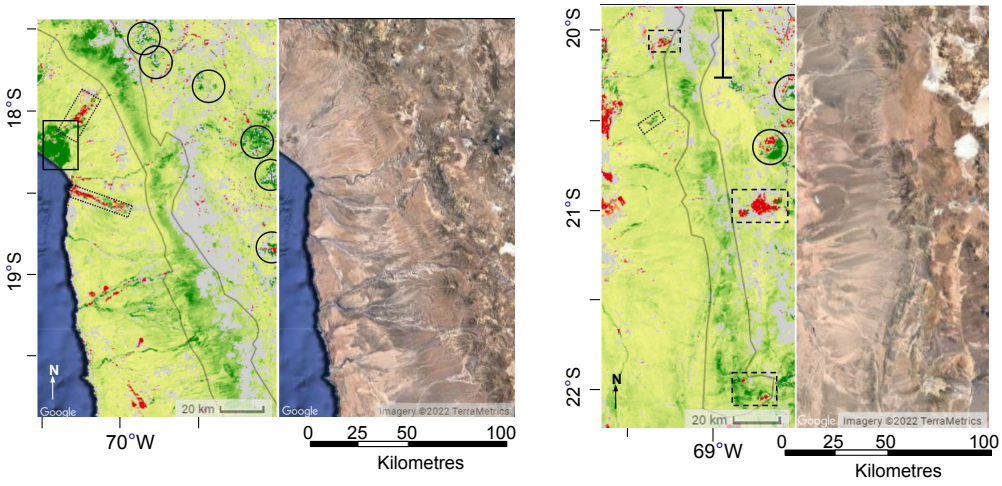

Figure 8. Dotted outlines denote urban areas and dashed outlines denote mines and quarries. Left: the greening of coastal vegetation, as shown in Figures 6 and 7, stops. Red or green lines extending from the coast up into the greening strip are rivers and roads. Right: between 19.9°S and 20.2°S, another gap in the greening strip can be found. South of this area, the greening of vegetation becomes less intense and the strip is no longer visible. Solid circles outline glaciers.

One of the more surprising results in this analysis is that the greening strip consistently ascends from north to south. At the most northern part of the region, around the Lambayeque area, greening occurs from 170 to 580 masl. In the southern region, around Chiquicamata, the same greening occurs between 2850 and 4250 masl. A visualisation of the relative EVI change for transects of equal latitude is shown in Figure 9. The data represented here include statistically significant trends within the area of interest, defined as the greening strip. The minimum, maximum and mean altitude for the greening strip increase as the latitude progresses southward. We also observe that the climate zones defined in the Köppen–Geiger model similarly ascend southwards but that the 'greening' strip does so more rapidly, crossing from lower elevation to higher elevation zones. The reason for this southward ascent remains unclear as the strip does not seem to follow isotherm or isohyet lines.

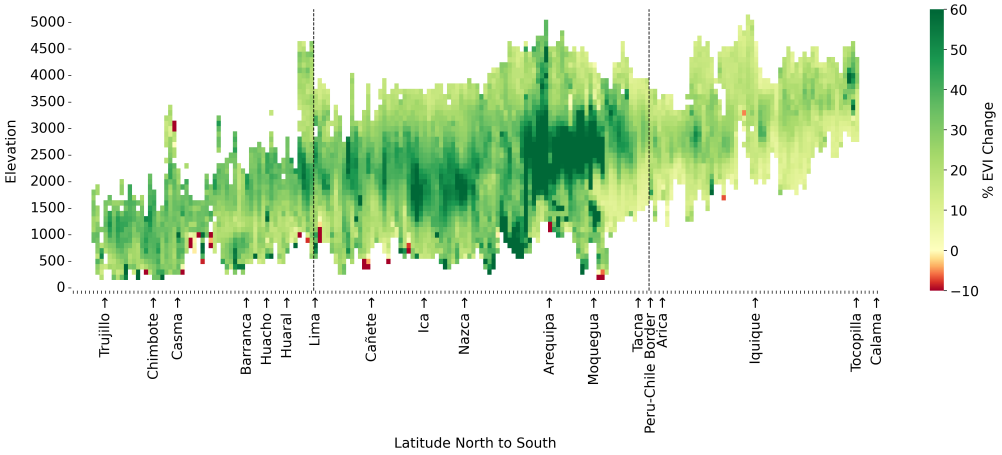

Figure 9. Visualisation of relative EVI change in the greening strip as a function of both latitude and altitude. Latitude cross-sections were taken from northern Peru to northern Chile. The greening gap described in Figure 4 can be observed between Casma and Barranca.

We compared the greening within the three main Köppen–Geiger zones in our region of interest (BWh, BWk, BSk) and compared the values of EVI change within and outside the area we define as the greening strip. Figure 10 shows a histogram of binned distributions of statistically significant pixel greening or browning. For each climate zone, the area

outside the greening strip contains a diverse set of EVI trends, both positive and negative, which sharply drops off after a positive trend greater than 30%. For pixels within the greening strip, however, there are almost no statistically significant browning pixels and the distribution is much more positive, with a dropoff around 50% relative EVI change.

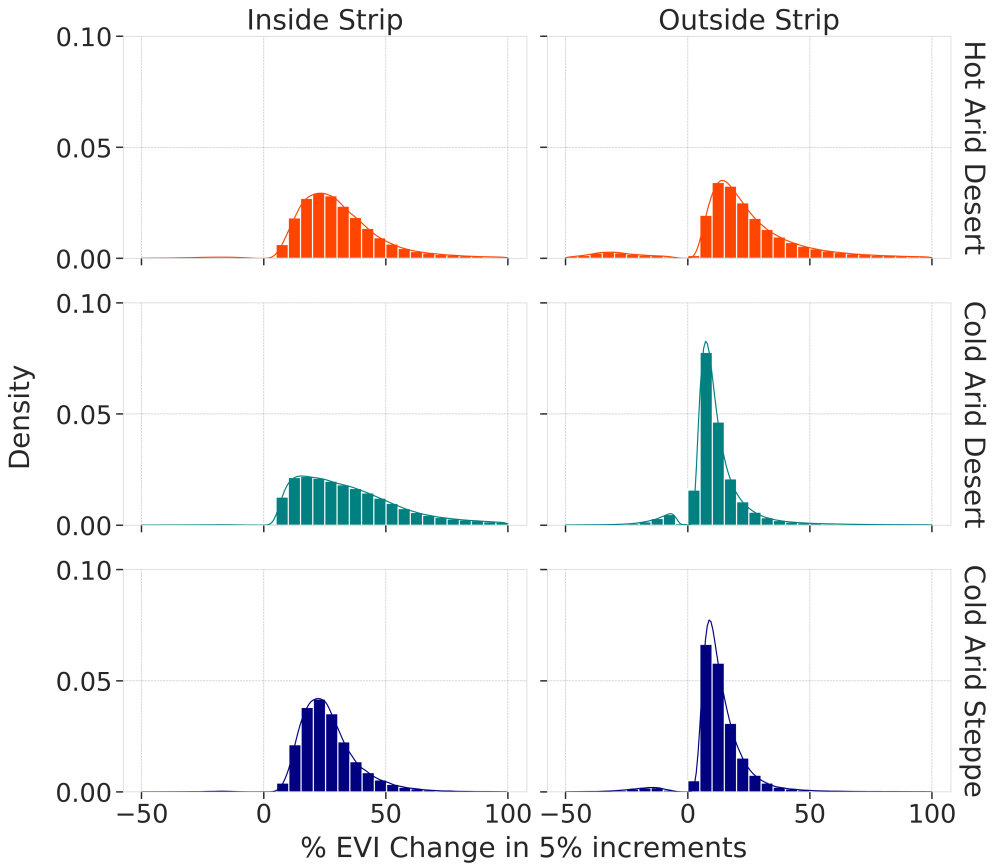

Figure 10. Binned distributions of statistically significant EVI changes.

The qualitative distribution of relative greening in Figure 10 shows that the vegetation within the greening strip behaves in a cohesive way across all three Köppen–Geiger zones. This is contrasted by the histograms comparing vegetation within a single Köppen–Geiger zone inside and outside of the greening strip.

Table 2 provides numerical correlations between the distributions represented in Figure 10. Here, we can clearly see that the areas defined by the greening strip in the cold arid desert (GS_BWk) and the greening strip in the cold arid steppe (GS_BSk) correlate more with each other than the areas of the same climate zones outside the greening strip. These results either indicate that the phenomenon contained within the greening strip does not follow previously defined climate zones or that the zones themselves need to be redefined in order to reflect the change in climatic conditions. The latter contradicts previous predictions by Beck et al., who claim that these climate zones will not change in the next 100 years [4]. The high correlation between the full greening strip (GS) and the sub-section that belongs to the cold arid desert (GS_BWk) exists because the greening strip is mostly located in that climate zone.

Table 2. Correlations between spatially averaged EVI time series within Köppen–Geiger climate zones. Cells highlighted in light grey represent correlations between the same climate zone inside vs. outside the greening strip; dark grey represents correlations between different zones inside the greening strip.

	BWk	BSk	GS	GS_BWh	GS_BWk	GS_BSk
BWh	0.85	0.82	0.72	0.92	0.71	0.59
BWk		0.79	0.63	0.78	0.60	0.54
BSk			0.69	0.79	0.67	0.64
GS				0.75	0.997	0.92
GS_BWh					0.72	0.60
GS_BWk						0.91

In addition to these previous observations, we observe intense greening in the coastal Lomas of Peru and Chile. The Lomas are coastal hills with a highly distinctive fog-dependent vegetation, exhibiting high levels of biological endemism. These fog-adapted plants produce a highly distinctive habitat constrained by the moisture content of coastal fog or Garua. They are found in the coastal deserts from central Peru to northern Chile from 5°S to 30°S. We observe that the greening in the coastal Lomas as well as that on the Pacific slope of the Andes is not directly anthropogenic in origin. We have not included the Lomas in our definition of the greening strip because they are both geographically separate and driven by different micro-climatic factors. We observe highly differentiated patterns of change below 1100 m in the coastal deserts, with greening hot spots associated with agricultural expansion and browning hot spots associated with urbanisation, mining, land slides and agricultural abandonment. These represent direct changes in land cover characteristics driven by human activity.

4. Discussion

We observe a continuous strip of greening along the Pacific slope that ascends from the hot desert in the north to the temperate zone (2500–3500 m) in the south with a 20-year increasing trend in EVI, representing a newly described regional phenomena. From this, we can deduce that changes in arid natural vegetation have occurred but not what this consists of in terms of species assemblages and the relative abundance of each species.

Although it is possible to subdivide the 20-year study period into 10 or 5 years and study short-term trends, this yields different results depending on how the period has been divided. The calculation method itself is skewed by the starting year: the result will be higher than real life if the starting year had relatively less vegetation. This could be the case if the period coincided with a particularly dry phase in the El Niño cycle. It is also possible that the observed 20-year trend is an anomalous phenomenon within much longer climatic cycles. As satellite data only cover the period from the 1980s, alternative datasets indicating vegetation changes would be needed to indicate whether these recent trends are part of such longer-term cycles or the consequence of more recent anthropogenic climate change. However, this result can form part of the basis of our interpretation of greening and browning trends in natural systems on the Pacific slope for which long-term study is required to monitor and confirm.

Exploring causality for this phenomenon is problematic since, as one moves south, the greening strip ascends, which would seem counterintuitive. That is, plant productivity would be expected to decline as temperature declines with increasing altitude and latitude, temperature being a primary limiting factor in photosynthesis.

The increase in global CO_2 contributes to the globally observed greening phenomenon and could account for greening inside and outside of the defined strip, but this cannot explain the shorter-term regionally determined fluctuations in EVI.

We must, therefore, look to moisture availability, the third driver in vegetation growth. Figure 11 and Table 3 show the correlations between the 20-year trend in EVI within the

greening strip and sea surface temperature (SST), precipitation and global CO_2 concentrations over the same time period.

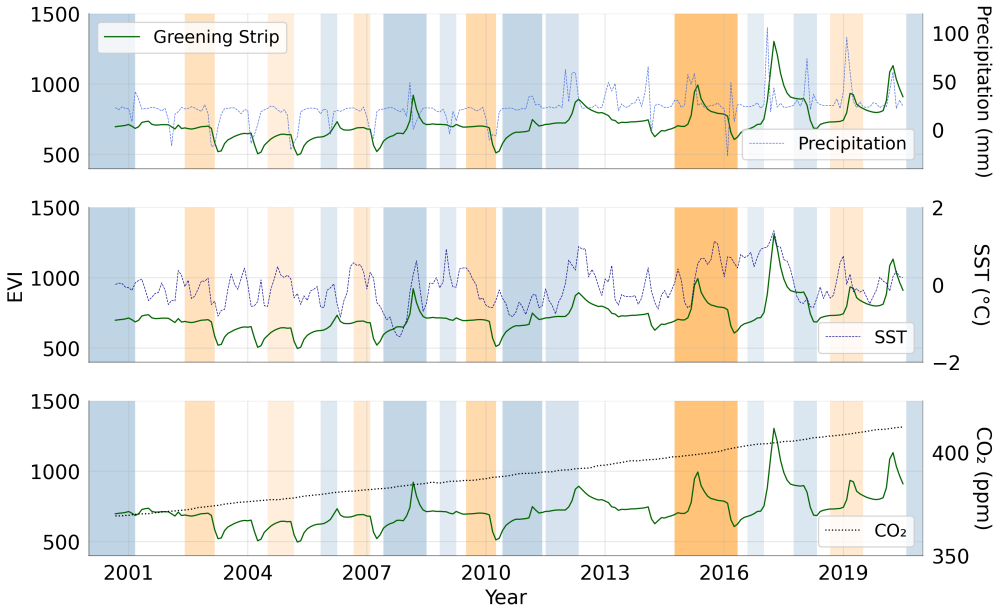

Figure 11. Monthly time series of spatially averaged EVI across the greening strip (solid dark green line) compared to monthly precipitation, sea surface temperature (SST) and atmospheric CO_2. Orange and blue shaded areas represent the duration of El Niño and La Niña events, respectively, where darker colours denote more intense events [81].

Table 3. Cross-correlation of the EVI time series in the greening strip and each Köppen–Geiger climate zone with precipitation, sea surface temperature and global CO_2 concentrations.

Region	Precipitation	SST	Global CO_2
BWh	0.65	0.26	0.93
BWk	0.36	0.18	0.85
BSk	0.28	0.19	0.77
GS	0.53	0.38	0.60
GS_BWh	0.57	0.27	0.83
GS_BWk	0.52	0.39	0.58
GS_BSk	0.45	0.37	0.46

When observing the correlations in Table 3, we focus on the relative correlations between each region rather than the actual values of each correlation. We note that there is more variation between the correlation of each climate zone outside the strip with precipitation, whereas, inside the strip, it is more similar. Outside the strip, there is less correlation with SST and higher correlation with CO_2 compared to inside the strip. It is important to note that, although we correlated distinct patterns in EVI with precipitation and temperature in a series of subdivisions, this only permits an initial examination of biogeophysical feedbacks and climatic drivers of vegetation response. We have not modelled vegetation dynamics to incorporate patterns of atmospheric circulation, the El Niño southern oscillation (ENSO) and regional and local topographical conditions, which lies beyond the scope of this paper.

When comparing the greening strip with land surface temperature (LST), we see complex patterns of warming and cooling across the Pacific slope and coastal deserts, with clearly differentiated and largely altitudinal micro-climatic zonation. It is to be expected that LST cooling is a consequence of increased vegetative productivity. However, it is not always the case that increased plant growth results in LST cooling, and we do observe a highly variegated patterning of cooling and warming across the Pacific slope in greening areas.

Understanding the geospatial relationship between LST and vegetation dynamics in the region requires a more in-depth analysis of regional climatological conditions. However, we cannot conclusively determine that LST is not a driver of vegetation growth in the greening strip since we also see Pacific slope warming highlighted by the Climate Change Institute's reanalyzer [82].

Although the complex geospatial interplay between LST and greening or browning is beyond the scope of this research paper, it is the subject of ongoing research, with this preliminary observation indicating that vegetation–climate feedback plays a complex role in vegetation dynamics if one is largely circumscribed by atmospheric circulation and oceanic currents.

5. Conclusions

We demonstrate that the greening strip is a statistically significant regional phenomenon. Although most likely driven by changes in the primary climatic variables that determine vegetative productivity, this is counterintuitive for several reasons. First, temperatures drop as one ascends, so vegetative productivity would be expected to decline, all else being equal. This was shown using simulated photosynthetic CO_2 uptake potential and altitude [37]. However, the greening strip behaves in the opposite direction, where the most intense relative greening rises in altitude as the strip progresses southward. Second, CO_2 concentration is a more generalised global driver but for the most part evenly distributed throughout the atmosphere. There is some altitudinal variation below 300 m that is associated with plant productivity and atmospheric stability, but the correlation of ground-level CO_2 concentrations and altitude is not significant above 800 m [38]. These previous results go against the clear delimitation of the greening strip. Third, although the novel phenomenon we describe is roughly located in the climate zones identified by the Köppen–Geiger climate classification system, this greening strip crosses from the hot arid desert through the cold arid desert into the cold arid steppe. This evolution through the climate zones as the greening strip extends from north to south indicates that the drivers of this positive EVI trend are not locked to a single climate zone and also do not span the entirety of climate zones as they are currently defined. This holds especially true for the hot arid desert and the cold arid steppe.

The identification and description of a novel greening phenomena, in an important but little-studied region, points to the critical need to fully understand the regional biogeophysical drivers and determinants of vegetation responses on the Pacific slope of Peru and northern Chile that mediate global increases in CO_2 concentration and temperature changes. These necessarily involve investigation into the complex relationships between regional topographic conditions, the El Nino (ENSO) phenomena and atmospheric circulation patterns driven by the north–south arrangement of the Andes.

Changes in regional biogeophysical dynamics will impact ecosystem integrity and thereby ecosystem processes in a highly water stressed region inhabited by significant populations and characterised by highly distinctive endemic species assemblages. Through the use of remote sensing techniques, we have identified a greening strip on the Pacific slope of the Andes that could herald significant impacts on both ecosystem services and biodiversity. The study highlights the need for regional studies in mountainous regions more widely to develop not only the efficacy of analysing remotely sensed data but also incorporating more robust ground-truthing methodologies to confirm the long-term impacts of climate change in sensitive regions vulnerable to changing climatic conditions.

Author Contributions: H.V.L. and E.K. curated, analyzed and visualized the satellite data from MODIS. E.B. analyzed the processed data for geographical significance. All authors discussed the climactic significance of the greening strip and made original contributions to the research. The paper was written by E.B., H.V.L. and E.K. with input from M.H. and C.H.W.B. C.H.W.B. managed the project. All authors have read and agreed to the published version of the manuscript.

Funding: This work was funded by Universidad Nacional de Cañete (UNDC), dpto Lima, Peru under grant agreement RG99980.

Data Availability Statement: Raw datasets are publicly available from MODIS or Google Earth Engine. Our processed data are available upon reasonable request to the corresponding authors.

Acknowledgments: We would like to thank Natalie Wetenhall for her numerous contributions to our discussions and Jorge Jhoncon Kooyip and Carlos Villanueva Aguilar at UNDC for their unfailing support and patience in the preparation of this manuscript. We also wish to thank John Forrest for careful proofreading of the manuscript, helpful discussions and general administrative support.

Conflicts of Interest: The authors declare no conflict of interest.

Abbreviations

The following abbreviations are used in this manuscript:

MDPI	Multidisciplinary Digital Publishing Institute
BWh	Hot arid desert
BWk	Cold arid desert
BSk	Cold arid steppe
BSh	Hot arid steppe
ET	Polar Tundra
GS	Greening Strip
NDVI	Normalized Difference Vegetation Index
EVI	Enhanced Vegetation Index
MODIS	Moderate Resolution Imaging Spectroradiometer
LSIB	Large Scale International Boundary
M–K	Mann–Kendall
ERA-5	European Centre for Medium-Range Weather Forecasts reanalysis
CHIRPS	Climate Hazards Group InfraRed Precipitation with Station
NOAA	National Oceanic and Atmospheric Administration
CGIAR	Consultative Group for International Agricultural Research
LCCS	Land Cover Classification System
FAO	Food and Agriculture Organisation
SST	Sea Surface Temperature
LST	Land Surface Temperature
ROI	Region of Interest
ITCZ	Intertropical Convergence Zone
ENSO	El Niño Southern Oscillation

References

1. Holdridge, L.R. Determination of world plant formations from simple climatic data. *Science* **1947**, *105*, 367–368. [CrossRef]
2. Kottek, M.; Grieser, J.; Beck, C.; Rudolf, B.; Rubel, F. World map of the Köppen-Geiger climate classification updated. *Meteorol. Z.* **2006**, *15*, 259–263. [CrossRef] [PubMed]
3. Köppen, W. Klassifikation der Klima nach Temperatur, Niederschlag und Jahreslauf. *Pet. Mitt.* **1918**, *64*, 243–248.
4. Beck, H.E.; Zimmermann, N.E.; McVicar, T.R.; Vergopolan, N.; Berg, A.; Wood, E.F. Present and future Köppen-Geiger climate classification maps at 1-km resolution. *Sci. Data* **2018**, *5*, 1–12. [CrossRef] [PubMed]
5. Drennan, P.M.; Nobel, P. Responses of CAM species to increasing atmospheric CO_2 concentrations. *Plant Cell Environ.* **2000**, *23*, 767–781. [CrossRef]
6. D'Odorico, P.; Laio, F.; Ridolfi, L. Vegetation patterns induced by random climate fluctuations. *Geophys. Res. Lett.* **2006**, *33*. [CrossRef]
7. Suc, J.P. Origin and evolution of the Mediterranean vegetation and climate in Europe. *Nature* **1984**, *307*, 429–432. [CrossRef]
8. Magyari, E.; Jakab, G.; Bálint, M.; Kern, Z.; Buczkó, K.; Braun, M. Rapid vegetation response to Lateglacial and early Holocene climatic fluctuation in the South Carpathian Mountains (Romania). *Quat. Sci. Rev.* **2012**, *35*, 116–130. [CrossRef]
9. Gitay, H.; Suárez, A.; Watson, R.T.; Dokken, D.J. *Climate Change and Biodiversity*; Intergovernmental Panel on Climate Change: Geneva, Switzerland, 2002.
10. Mooney, H.; Larigauderie, A.; Cesario, M.; Elmquist, T.; Hoegh-Guldberg, O.; Lavorel, S.; Mace, G.M.; Palmer, M.; Scholes, R.; Yahara, T. Biodiversity, climate change, and ecosystem services. *Curr. Opin. Environ. Sustain.* **2009**, *1*, 46–54. [CrossRef]
11. Scholes, R.J. Climate change and ecosystem services. *Wiley Interdiscip. Rev. Clim. Chang.* **2016**, *7*, 537–550. [CrossRef]

12. Song, X.P.; Hansen, M.C.; Stehman, S.V.; Potapov, P.V.; Tyukavina, A.; Vermote, E.F.; Townshend, J.R. Global land change from 1982 to 2016. *Nature* **2018**, *560*, 639–643. [CrossRef]
13. NOAA. Global Monitoring Laboratory—Carbon Cycle Greenhouse Gases. 2022. Available online: https://gml.noaa.gov/ccgg/trends/global.html (accessed on 26 April 2023).
14. Joos, F.; Spahni, R. Rates of change in natural and anthropogenic radiative forcing over the past 20,000 years. *Proc. Natl. Acad. Sci. USA* **2008**, *105*, 1425–1430. [CrossRef]
15. Friedlingstein, P.; Jones, M.W.; O'Sullivan, M.; Andrew, R.M.; Bakker, D.C.; Hauck, J.; Le Quéré, C.; Peters, G.P.; Peters, W.; Pongratz, J.; et al. Global carbon budget 2021. *Earth Syst. Sci. Data* **2022**, *14*, 1917–2005. [CrossRef]
16. Ralph Keeling, R.; Tans, P. Trends in Atmospheric Carbon Dioxide, Mauna Loa CO_2 Monthly Mean Data. Available online: https://gml.noaa.gov/ccgg/trends/ (accessed on 22 March 2022).
17. Piao, S.; Wang, X.; Park, T.; Chen, C.; Lian, X.; He, Y.; Bjerke, J.W.; Chen, A.; Ciais, P.; Tømmervik, H.; et al. Characteristics, drivers and feedbacks of global greening. *Nat. Rev. Earth Environ.* **2020**, *1*, 14–27. [CrossRef]
18. Morison, J.; Lawlor, D. Interactions between increasing CO_2 concentration and temperature on plant growth. *Plant Cell Environ.* **1999**, *22*, 659–682. [CrossRef]
19. Mishra, N.B.; Mainali, K.P. Greening and browning of the Himalaya: Spatial patterns and the role of climatic change and human drivers. *Sci. Total Environ.* **2017**, *587*, 326–339. [CrossRef] [PubMed]
20. Young, B.; Young, K.R.; Josse, C. Vulnerability of tropical Andean ecosystems to climate change. In *Climate Change and Biodiversity in the Tropical Andes*; SCOPE, IAI: Lod, Israel, 2011; pp. 170–181.
21. Prieto-Torres, D.A.; Lira-Noriega, A.; Navarro-Sigüenza, A.G. Climate change promotes species loss and uneven modification of richness patterns in the avifauna associated to Neotropical seasonally dry forests. *Perspect. Ecol. Conserv.* **2020**, *18*, 19–30. [CrossRef]
22. Ruhm, J.; Böhnert, T.; Weigend, M.; Merklinger, F.F.; Stoll, A.; Quandt, D.; Luebert, F. Plant life at the dry limit—Spatial patterns of floristic diversity and composition around the hyperarid core of the Atacama Desert. *PLoS ONE* **2020**, *15*, e0233729. [CrossRef] [PubMed]
23. Romero, H.; Ordenes, F. Emerging urbanization in the Southern Andes. *Mt. Res. Dev.* **2004**, *24*, 197–201. [CrossRef]
24. Nottingham, A.T.; Turner, B.L.; Whitaker, J.; Ostle, N.; Bardgett, R.D.; McNamara, N.P.; Salinas, N.; Meir, P. Temperature sensitivity of soil enzymes along an elevation gradient in the Peruvian Andes. *Biogeochemistry* **2016**, *127*, 217–230. [CrossRef]
25. Horgan, F.G. Effects of deforestation on diversity, biomass and function of dung beetles on the eastern slopes of the Peruvian Andes. *For. Ecol. Manag.* **2005**, *216*, 117–133. [CrossRef]
26. Bax, V.; Francesconi, W. Environmental predictors of forest change: An analysis of natural predisposition to deforestation in the tropical Andes region, Peru. *Appl. Geogr.* **2018**, *91*, 99–110. [CrossRef]
27. Barnes, E.P.; Hunter, M.A.; Lepage, H.V.; Luján, H.E.V.; Jamanca, N.C. The avifauna of the río Fortaleza drainage basin, dptos. Lima and Ancash, Peru. *Cotinga* **2022**, *44*, 43–59.
28. Best, B.; Kessler, M. *Biodiversity and Conservation in Tumbesian Ecuador and Peru*; BirdLife International: Cambridge, UK, 1995; Volume 218.
29. Devenish, C.; Nuñez Cortez, E.; Buchanan, G.; Smith, G.R.; Marsden, S.J. Estimating ecological metrics for holistic conservation management in a biodiverse but information-poor tropical region. *Conserv. Sci. Pract.* **2020**, *2*, e153. [CrossRef]
30. Stattersfield, A.J. *Endemic Bird Areas of the World-Priorities for Biodiversity Conservation*; Bird Life International: Cambridge, UK, 1998.
31. Ioris, A.A. Water scarcity and the exclusionary city: The struggle for water justice in Lima, Peru. *Water Int.* **2016**, *41*, 125–139. [CrossRef]
32. Salmoral, G.; Zegarra, E.; Vázquez-Rowe, I.; González, F.; Del Castillo, L.; Saravia, G.R.; Graves, A.; Rey, D.; Knox, J.W. Water-related challenges in nexus governance for sustainable development: Insights from the city of Arequipa, Peru. *Sci. Total Environ.* **2020**, *747*, 141114. [CrossRef]
33. Fragkou, M.C.; McEvoy, J. Trust matters: Why augmenting water supplies via desalination may not overcome perceptual water scarcity. *Desalination* **2016**, *397*, 1–8. [CrossRef]
34. Arp, W. Effects of source-sink relations on photosynthetic acclimation to elevated CO_2. *Plant Cell Environ.* **1991**, *14*, 869–875. [CrossRef]
35. Lawlor, D.; Mitchell, R. The effects of increasing CO_2 on crop photosynthesis and productivity: A review of field studies. *Plant Cell Environ.* **1991**, *14*, 807–818. [CrossRef]
36. Morison, J.I.; Morecroft, M.D. *Plant Growth and Climate Change*; John Wiley & Sons: Hoboken, NJ, USA, 2008.
37. Smith, W.; Donahue, R. Simulated influence of altitude on photosynthetic CO_2 uptake potential in plants. *Plant Cell Environ.* **1991**, *14*, 133–136. [CrossRef]
38. Li, Y.; Deng, J.; Mu, C.; Xing, Z.; Du, K. Vertical distribution of CO_2 in the atmospheric boundary layer: Characteristics and impact of meteorological variables. *Atmos. Environ.* **2014**, *91*, 110–117. [CrossRef]
39. Rau, P.; Bourrel, L.; Labat, D.; Melo, P.; Dewitte, B.; Frappart, F.; Lavado, W.; Felipe, O. Regionalization of rainfall over the Peruvian Pacific slope and coast. *Int. J. Climatol.* **2017**, *37*, 143–158. [CrossRef]
40. Sanabria, J.; Bourrel, L.; Dewitte, B.; Frappart, F.; Rau, P.; Solis, O.; Labat, D. Rainfall along the coast of Peru during strong El Niño events. *Int. J. Climatol.* **2018**, *38*, 1737–1747. [CrossRef]
41. Campbell, J.B.; Wynne, R.H. *Introduction to Remote Sensing*; Guilford Press: New York City, NY, USA, 2011.

42. Xie, Y.; Sha, Z.; Yu, M. Remote sensing imagery in vegetation mapping: A review. *J. Plant Ecol.* **2008**, *1*, 9–23. [CrossRef]
43. Cortés, J.; Mahecha, M.D.; Reichstein, M.; Myneni, R.B.; Chen, C.; Brenning, A. Where are global vegetation greening and browning trends significant? *Geophys. Res. Lett.* **2021**, *48*, e2020GL091496. [CrossRef]
44. Pettorelli, N.; Vik, J.O.; Mysterud, A.; Gaillard, J.M.; Tucker, C.J.; Stenseth, N.C. Using the satellite-derived NDVI to assess ecological responses to environmental change. *Trends Ecol. Evol.* **2005**, *20*, 503–510. [CrossRef]
45. Wardlow, B.D.; Egbert, S.L. A comparison of MODIS 250-m EVI and NDVI data for crop mapping: A case study for southwest Kansas. *Int. J. Remote Sens.* **2010**, *31*, 805–830. [CrossRef]
46. Huete, A.R.; Didan, K.; Shimabukuro, Y.E.; Ratana, P.; Saleska, S.R.; Hutyra, L.R.; Yang, W.; Nemani, R.R.; Myneni, R. Amazon rainforests green-up with sunlight in dry season. *Geophys. Res. Lett.* **2006**, *33*. [CrossRef]
47. Verbyla, D. The greening and browning of Alaska based on 1982–2003 satellite data. *Glob. Ecol. Biogeogr.* **2008**, *17*, 547–555. [CrossRef]
48. Parent, M.B.; Verbyla, D. The browning of Alaska's boreal forest. *Remote Sens.* **2010**, *2*, 2729–2747. [CrossRef]
49. Bhatt, U.S.; Walker, D.A.; Raynolds, M.K.; Comiso, J.C.; Epstein, H.E.; Jia, G.; Gens, R.; Pinzon, J.E.; Tucker, C.J.; Tweedie, C.E.; et al. Circumpolar Arctic tundra vegetation change is linked to sea ice decline. *Earth Interact.* **2010**, *14*, 1–20. [CrossRef]
50. Aide, T.M.; Grau, H.R.; Graesser, J.; Andrade-Nuñez, M.J.; Aráoz, E.; Barros, A.P.; Campos-Cerqueira, M.; Chacon-Moreno, E.; Cuesta, F.; Espinoza, R.; et al. Woody vegetation dynamics in the tropical and subtropical Andes from 2001 to 2014: Satellite image interpretation and expert validation. *Glob. Chang. Biol.* **2019**, *25*, 2112–2126. [CrossRef]
51. Carlson, B.Z.; Corona, M.C.; Dentant, C.; Bonet, R.; Thuiller, W.; Choler, P. Observed long-term greening of alpine vegetation—A case study in the French Alps. *Environ. Res. Lett.* **2017**, *12*, 114006. [CrossRef]
52. Polk, M.H.; Mishra, N.B.; Young, K.R.; Mainali, K. Greening and Browning Trends across Peru's Diverse Environments. *Remote Sens.* **2020**, *12*, 2418. [CrossRef]
53. Zhang, Y.; Song, C.; Band, L.E.; Sun, G.; Li, J. Reanalysis of global terrestrial vegetation trends from MODIS products: Browning or greening? *Remote Sens. Environ.* **2017**, *191*, 145–155. [CrossRef]
54. Saleska, S.R.; Wu, J.; Guan, K.; Araujo, A.C.; Huete, A.; Nobre, A.D.; Restrepo-Coupe, N. Dry-season greening of Amazon forests. *Nature* **2016**, *531*, E4–E5. [CrossRef] [PubMed]
55. Morton, D.C.; Nagol, J.; Carabajal, C.C.; Rosette, J.; Palace, M.; Cook, B.D.; Vermote, E.F.; Harding, D.J.; North, P.R. Amazon forests maintain consistent canopy structure and greenness during the dry season. *Nature* **2014**, *506*, 221–224. [CrossRef] [PubMed]
56. Sylvester, S.P.; Sylvester, M.D.; Kessler, M. Inaccessible ledges as refuges for the natural vegetation of the high Andes. *J. Veg. Sci.* **2014**, *25*, 1225–1234. [CrossRef]
57. Valencia, B.G.; Bush, M.B.; Coe, A.L.; Orren, E.; Gosling, W.D. Polylepis woodland dynamics during the last 20,000 years. *J. Biogeogr.* **2018**, *45*, 1019–1030. [CrossRef]
58. Rundel, P.W.; Dillon, M.O.; Palma, B.; Mooney, H.A.; Gulmon, S.; Ehleringer, J. The phytogeography and ecology of the coastal Atacama and Peruvian deserts. *Aliso J. Syst. Florist. Bot.* **1991**, *13*, 1–49. [CrossRef]
59. Sulca, J.; Takahashi, K.; Espinoza, J.C.; Vuille, M.; Lavado-Casimiro, W. Impacts of different ENSO flavors and tropical Pacific convection variability (ITCZ, SPCZ) on austral summer rainfall in South America, with a focus on Peru. *Int. J. Climatol.* **2018**, *38*, 420–435. [CrossRef]
60. Fjeldså, J. The avifauna of the Polylepis woodlands of the Andean highlands: The efficiency of basing conservation priorities on patterns of endemism. *Bird Conserv. Int.* **1993**, *3*, 37–55. [CrossRef]
61. Justice, C.O.; Vermote, E.; Townshend, J.R.; Defries, R.; Roy, D.P.; Hall, D.K.; Salomonson, V.V.; Privette, J.L.; Riggs, G.; Strahler, A.; et al. The Moderate Resolution Imaging Spectroradiometer (MODIS): Land remote sensing for global change research. *IEEE Trans. Geosci. Remote Sens.* **1998**, *36*, 1228–1249. [CrossRef]
62. Didan, K. MOD13Q1 MODIS/Terra Vegetation Indices 16-Day L3 Global 250 m SIN Grid V006. 2015. Available online: https://lpdaac.usgs.gov/products/mod13q1v006/ (accessed on 26 April 2023).
63. Validation at Stage 3 Has Been Achieved for the MODIS Vegetation Index (VI) Product Suite. Available online: https://modis-land.gsfc.nasa.gov/ValStatus.php?ProductID=MOD13 (accessed on 26 April 2023).
64. Gorelick, N.; Hancher, M.; Dixon, M.; Ilyushchenko, S.; Thau, D.; Moore, R. Google Earth Engine: Planetary-scale geospatial analysis for everyone. *Remote Sens. Environ.* **2017**, *202*, 18–27. [CrossRef]
65. Didan, K.; Munoz, A.B.; Solano, R.; Huete, A. MODIS Vegetation Index User's Guide (MOD13 Series) Version 3.00, June 2015 (Collection 6), 2015.
66. Rousseeuw, P.J.; Leroy, A.M. *Robust Regression and Outlier Detection*; John Wiley & Sons: Hoboken, NJ, USA, 2005.
67. Seabold, S.; Perktold, J. statsmodels: Econometric and statistical modeling with python. In Proceedings of the 9th Python in Science Conference, Austin, TX, USA, 28 June–3 July 2010.
68. Chen, J.; Jönsson, P.; Tamura, M.; Gu, Z.; Matsushita, B.; Eklundh, L. A simple method for reconstructing a high-quality NDVI time-series data set based on the Savitzky–Golay filter. *Remote Sens. Environ.* **2004**, *91*, 332–344. [CrossRef]
69. Whittaker, E.T. On a New Method of Graduation. *Proc. Edinb. Math. Soc.* **1922**, *41*, 63–75. [CrossRef]
70. Eilers, P.H. A perfect smoother. *Anal. Chem.* **2003**, *75*, 3631–3636. [CrossRef]
71. Mann, H.B. Nonparametric tests against trend. *Econom. J. Econom. Soc.* **1945**, *13*, 245–259. [CrossRef]
72. Kendall, M.G. *Rank Correlation Methods*; Griffin Press: Salisbury, Australia, 1948.
73. Theil, H. A Rank-Invariant Method of Linear and Polynomial Regression Analysis. *Indag. Math.* **1950**, *12*, 173.

74. Sen, P.K. Estimates of the regression coefficient based on Kendall's tau. *J. Am. Stat. Assoc.* **1968**, *63*, 1379–1389. [CrossRef]
75. Conover, W.J. *Practical Nonparametric Statistics*; John Wiley & Sons: Hoboken, NJ, USA, 1999; Volume 350.
76. Hussain, M.; Mahmud, I. pyMannKendall: A python package for non parametric Mann Kendall family of trend tests. *J. Open Source Softw.* **2019**, *4*, 1556. [CrossRef]
77. Copernicus Global Land Operations "Vegetation and Energy"—MODERATE DYNAMIC LAND COVER 100M VERSION (COLLECTION) 3. Available online: https://land.copernicus.eu/global/sites/cgls.vito.be/files/products/CGLOPS1_PUM_LC100m-V3_I3.4.pdf (accessed on 26 April 2023).
78. UC Santa Barbara, UCSB CHG. CHIRPS Daily: Climate Hazards Group InfraRed Precipitation with Station Data (Version 2.0 Final). Available online: https://developers.google.com/earth-engine/datasets/catalog/UCSB-CHG_CHIRPS_DAILY#bands (accessed on 26 April 2023).
79. Hersbach, H.; Bell, B.; Berrisford, P.; Biavati, G.; Horányi, A.; Muñoz Sabater, J.; Nicolas, J.; Peubey, C.; Radu, R.; Rozum, I.; et al. ERA5 Monthly Averaged Data on Single Levels from 1979 to Present. 2019. Available online: https://doi.org/10.24381/cds.f17050d7 (accessed on 26 April 2023).
80. Dlugokencky, E.; Tans, P. Trends in Atmospheric Carbon Dioxide, Globally Averaged Marine Surface Monthly Mean Data. Available online: https://gml.noaa.gov/ccgg/trends/ (accessed on 22 March 2022).
81. Center, N.C.P. NOAA's Climate Prediction Center. 2001. Available online: https://origin.cpc.ncep.noaa.gov/products/analysis_monitoring/ensostuff/ONI_v5.php (accessed on 26 April 2023).
82. Birkel, S. About Climate Reanalyzer. Available online: https://climatereanalyzer.org/about/ (accessed on 26 April 2023).